Valley-conserved topological integrated antenna for 100-Gbps THz 6G wireless

Ridong Jia, Sonu Kumar, Thomas Caiwei Tan, Abhishek Kumar, Yi Ji Tan, Manoj Gupta, Pascal Szriftgiser, Arokiaswami Alphones, Guillaume Ducournau, Ranjan Singh

PHYSICS

Valley-conserved topological integrated antenna for 100-Gbps THz 6G wireless

Ridong Jia[1,2], Sonu Kumar[3], Thomas Caiwei Tan[1,2], Abhishek Kumar[1,2], Yi Ji Tan[1,2], Manoj Gupta[1,2], Pascal Szriftgiser[4], Arokiaswami Alphones[3], Guillaume Ducournau[5], Ranjan Singh[1,2]*

The topological phase revolutionized wave transport, enabling integrated photonic interconnects with sharp light bending on a chip. However, the persistent challenge of momentum mismatch during intermedium topological mode transitions due to material impedance inconsistency remains. We present a 100-Gbps topological wireless communication link using integrated photonic devices that conserve valley momentum. The valley-conserved silicon topological waveguide antenna achieves a 12.2-dBi gain, constant group delay across a 30-GHz bandwidth and enables active beam steering within a 36° angular range. The complementary metal oxide semiconductor–compatible valley-conserved devices represent a major milestone in hybrid electronic-photonic-based topological wireless communications, enabling terabit-per-second backhaul communication, high throughput, and intermedium transport of information carriers, vital for the future of communication from the sixth to X generation.

INTRODUCTION

The topological edge state is a highly conductive state that exists at the edge of topological insulating bulk, and it has been shown to facilitate the efficient transport of electrons (*1*, *2*), photons (*3*, *4*), and acoustic waves (*5*). Photonic topological insulators (PTIs) (*3*, *4*) have garnered notable attention as a prominent area of research in the past decade, owing to their potential as a robust electromagnetic platform featuring remarkably low bending loss and backscattering immunity. Among various PTIs, valley photonic crystal (VPC) (*6*, *7*) offers an intriguing valley momentum for robust transport of waves at chip scale (*8*, *9*) without the need for an external magnetic field. VPCs have been used to develop numerous efficient topo-devices for photonic integrated circuits including topological waveguides (*6*, *10*, *11*), beam splitters (*12*, *13*), cavities (*14*, *15*), and lasers (*16*, *17*). However, present topological photonic chip designs are mostly demonstrated on a single topological platform with a lack of focus on the coupling of electromagnetic waves in and out of the topological chip. This is attributed to the substantial momentum mismatch due to the refractive index contrast when transitioning topological states between distinct topological chips or radiating electromagnetic waves from the chip to free space and vice versa.

Here, we propose a mechanism for valley momentum conservation that addresses the problem of inefficient interchip topological mode transition over the air. We experimentally validate the concept by using a terahertz wireless communication link that uses topological devices to efficiently convert electromagnetic waves between an all-silicon VPC chip and free space, where there are large differences in the effective refractive indices. Compared to conventional terahertz photonic crystal waveguides (*18*–*20*), the topologically protected robust transport and broadband linear dispersion of the used VPC enables on-chip data communication with high speed and is immune to bends and backscattering (*8*, *21*, *22*). An efficient over-the-air link of such advanced on-chip modes in the terahertz band allows the conservation of valley momentum between chips and is expected to drive the high-speed wireless communication from sixth to X generation (6G to XG), with the potential to assist the next generation of industrial revolution in decades (*18*, *23*–*28*).

RESULTS

Figure 1A depicts our proposed terahertz topological wireless communication link between all-silicon VPC chips using the proposed high-gain topological antenna (TA) at both the transmitter (Tx-TA) and receiver (Rx-TA) ends, which achieves a remarkable 100-Gbps data rate at a 1.2-cm over-the-air distance. Each TA device is composed of an on-chip VPC waveguide that supports valley-dependent kink states (*6*, *8*), and a semi-circular graded refractive index buffer (GRIB). The GRIB design effectively mitigated the considerable momentum difference caused by the large refractive index contrast. GRIB is shown in Fig. 1 (B and C) by the zoomed images of the VPC-adjacent and the edge regions of GRIB, as indicated by GRIB-I and GRIB-II, respectively. Illustrated in Fig. 1B, GRIB and VPC are integrated via one-time deep etching on a silicon wafer with multiple aspect ratios (see Materials and Methods). The VPC unit cell is in a hexagonal lattice (white hexagon) with equilateral triangular holes of different sizes, which breaks the inversion symmetry. The VPC waveguide is designed by interfacing two mirrored bulk slabs with opposite valley Chern numbers (fig. S1). GRIB is a photonic crystal with hexagonal air holes in a triangular lattice, of which the period is half of the VPC. Thus, GRIB is regarded as an

[1]Division of Physics and Applied Physics, School of Physical and Mathematical Sciences, Nanyang Technological University, 21 Nanyang Link, Singapore 637371, Singapore. [2]Centre for Disruptive Photonic Technologies, The Photonics Institute, Nanyang Technological University, 21 Nanyang Link, Singapore 637371, Singapore. [3]School of Electrical and Electronic Engineering, Nanyang Technological University, 50 Nanyang Ave, Singapore 639798, Singapore. [4]Laboratoire de Physique des Lasers, Atomes et Molécules, PhLAM, UMR 8523, Université de Lille, CNRS, 59655 Villeneuve d'Ascq, France. [5]Institut d'Electronique de Microélectronique et de Nanotechnologie, Université de Lille 1, Lille, France.
*Corresponding author. Email: ranjans@ntu.edu.sg

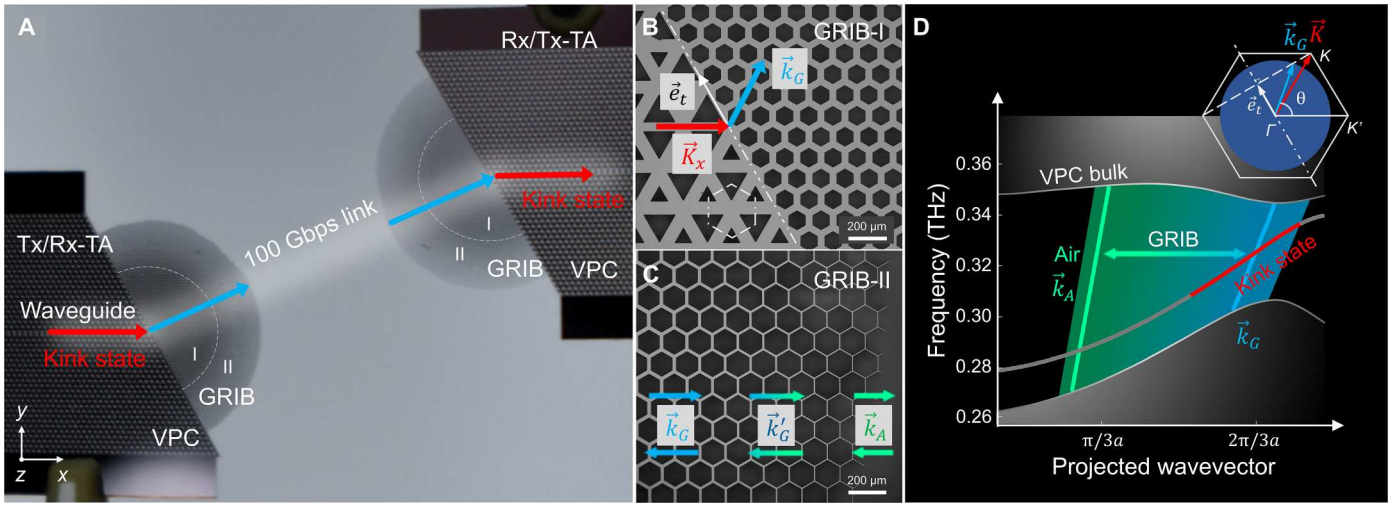

Fig. 1. Interchip topological wireless communication link via momentum-conserved silicon devices. (**A**) Top view of terahertz wireless link between valley photonic crystal (VPC) chips achieving a 100-Gbps data rate. Tx-TA and Rx-TA are identical consisting of on-chip VPC waveguide with topological kink state and GRIB including regions I and II for efficient momentum matching. (**B**) Optical image of the GRIB-I region, where the projected valley momentum $\vec{K}_x$ (red) is coupled into the mode in GRIB with momentum $\vec{k}_G$ (blue) at the VPC-GRIB interface (white dashed line, the tangential direction is $\vec{e}_t$). The VPC consists of triangular holes in the hexagonal unit cell (white hexagon) with broken inversion symmetry, while GRIB is a trivial photonic crystal in a triangular lattice with hexagonal holes. (**C**) Optical image of the GRIB-II region. The spatially changing hole sizes create the graded refractive index where the momentum adiabatically transforms from $\vec{k}_G$ to $\vec{k}'_G$, and eventually reaches air with momentum $\vec{k}_A$ (rightward arrows) and vice versa (leftward arrows). (**D**) Numerical dispersion diagrams of VPC kink state (red) and eigenmodes in GRIB (gradient region) and air (green), as projected into the $\vec{e}_t$ direction. The kink state is coupled into GRIB at the intersection point, represented at central frequency, and the adiabatic changing momenta (colored region) bridge the kink state with plane wave in the air. Each mode exhibits broadband linear dispersion. The momentum matching at the intersection point is shown in the top-right inset in the momentum space with the Brillouin zone (hexagon) of VPC. The magnitude of GRIB momentum $|\vec{k}_G|$ (blue circle) is determined by the effective refractive index of GRIB, and the beam direction θ relies on the matching of $\vec{K}$ (red) and $\vec{k}_G$ (blue).

effective medium in the frequency band of interest. The meticulously designed hole sizes allow an effective refractive index n to match the VPC membrane (see Supplementary Materials). At the 120° oriented VPC-GRIB interface (white dashed line), of which the tangential direction is $\vec{e}_t$, the kink state with projected valley momentum $\vec{K}_x$ (red arrow) is coupled into the mode in GRIB with momentum $\vec{k}_G$ (blue arrow). In the GRIB-II region as shown in Fig. 1C, graded n along the radial direction is achieved by spatially varying the GRIB hole size, which enables the adiabatically changing momentum $\vec{k}'_G$ (gradient arrow) to bridge $\vec{k}_G$ and momentum in air $\vec{k}_A$ (green arrow) for efficiently radiating on-chip kink state and vice versa. The necessity of the GRIB design is also discussed in the Supplementary Materials (figs. S2 and S3).

The numerical dispersion diagrams of the VPC kink state (red), eigen modes in GRIB (blue), and plane wave in air (green) are shown in Fig. 1D, as projected onto $\vec{e}_t$, illustrating the overall mode transition of the TA. The momentum matching at the VPC-GRIB interface is depicted by the intersection point of the K-valley kink state and GRIB-I mode (blue line) as represented at the center frequency, while the adiabatic evolution of wave from GRIB-I to GRIB-II is indicated by the gradient-colored region, bridging the gap of topological mode and free space wave. The topological-trivial momentum matching at the VPC-GRIB interface is also shown in the momentum space with the Brillouin zone of VPC (hexagon) in the top-right inset of Fig. 1D. Valley momentum at the VPC-GRIB interface is along the K direction, of which the amplitude is $|\vec{K}| = 4\pi/3a$ at center frequency (a is the VPC lattice constant). The amplitude of momentum in GRIB is $|\vec{k}_G| = \omega n(\vec{r})/c$ [ω is the angular frequency, $n(\vec{r})$ is the effective refractive index of GRIB at position $\vec{r}$, and c is the light speed in vacuum] as indicated by the blue circle. The beam direction θ is determined by the phase matching equation (*29*) as $\vec{K} \cdot \vec{e}_t = \vec{k}_G \cdot \vec{e}_t$ based on the electromagnetic continuity at the VPC-GRIB interface. The band crossing at other frequencies within the topological bandgap can be achieved at different angles θ(ω) based on this frequency-dependent matching condition. The overall mode conversion for Tx-TA is represented by the equation $\vec{K} \cdot \vec{e}_t = \vec{k}_G \cdot \vec{e}_t \rightarrow \vec{k}' \cdot \vec{e}_t = \vec{k}_A \cdot \vec{e}_t$, while the opposite holds true for Rx-TA. The constant group velocity exhibited by the linear dispersion of each mode in Fig. 1D is crucial in ensuring the simultaneous delivery of modulated symbols across the entire bandwidth, for terabit-per-second data transmission between chips.

The VPC waveguide is interfaced by two mirrored bulk slabs with opposite valley Chern numbers of ±1/2, respectively (*6*). Figure 2A shows the used VPC unit cells with equilateral triangular holes of side lengths l_1 and l_2 and lattice constant a = 250 μm, which supports the transverse electric (TE) mode. The asymmetric geometrical parameter for inversion-symmetry breaking, defined as $\delta = l_1 - l_2$, differentiates the type A ($\delta = +0.3a$) and type B ($\delta = -0.3a$) unit cells. The topological eigenstates with the intrinsic phase singularities are shown by the argument of the out-of-plane magnetic field $\arg(\vec{H}_z)$ (blue colormap) at K valley. The in-plane Poynting vector $\vec{S}$ (black arrow) also exhibits a vortex feature and has opposite chirality for type A and type B unit cells. The kink state occurs at the

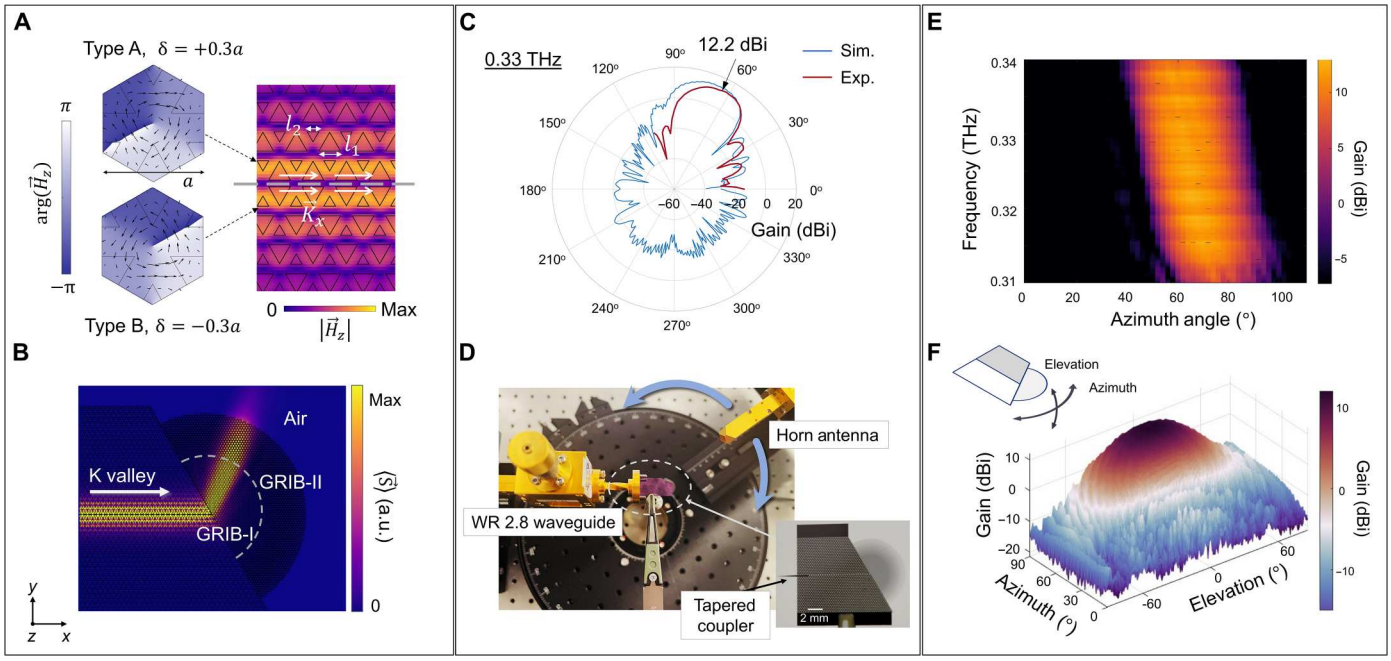

Fig. 2. Valley-conserved TA measurements. (**A**) VPC unit cell (left) and topological kink state (right). The inversion symmetry is broken by varying the side lengths of the equilateral triangular air holes, l_1 and l_2. The topological eigen vortices are shown by the simulated phase singularity of the out-of-plane magnetic field $\arg(\vec{H}_z)$ (blue colormap) and vortex Poynting vector $\vec{S}$ (black arrows). The symmetry breaking strength $\delta = l_1 - l_2$ are $+0.3a$ and $-0.3a$ (a is the lattice constant) for type A and B unit cells, respectively. The topological kink state exists at the interface (gray dashed line) formed by two inversed VPC bulks as depicted by the simulated $|\vec{H}_z|$ (yellow colormap). (**B**) Simulated power flow $\langle\vec{S}\rangle$ of TA. The terahertz beam in the VPC interface is coupled into GRIB-I and GRIB-II and finally radiated into the air. (**C**) Simulated and measured radiation patterns of TA. The measured maximum gain is 12.2 dBi at azimuth angle θ_M of 62.7° at 0.33 THz. (**D**) Experimental setup and top view of the TA device. The terahertz signal is coupled to the antenna via a standard WR 2.8 waveguide into a tapered coupler attached to the silicon chip, and the receiving WR 2.8 horn antenna mounted on a rotational stage scans the power of each azimuthal angle in a far-field distance of 4.5 cm. (**E**) Gain spectra, showing a nearly constant gain of 12.2 dBi from 0.31 to 0.34 THz. (**F**) 3D antenna radiation spectrum.

interface (gray dashed line) within the bandgap surrounded by type A and type B bulk structures as shown by the simulated $|\vec{H}_z|$ (yellow colormap). Figure 2B illustrates the simulated power flow $\langle\vec{S}\rangle$ of the TA chip with the efficient mode coupling process from VPC waveguide to GRIB-I and GRIB-II, and eventually reaching air.

The momentum matching achieved by the proposed topological devices allows high-gain radiation. Figure 2C shows the simulated (blue) and experimentally measured (red) far-field radiation patterns against the azimuth angle θ for the TA. We record the maximum gain of 12.2 dBi at the azimuth angle $\theta_M = 62°$ at 0.33 THz, which matches the simulation result of 13.5 dBi at $\theta_M = 62.28°$. The half-maximum-gain angle width (HMAW) of the device is 25°. The terahertz wave is coupled into the TA chip with a standard WR 2.8 hollow waveguide and the silicon tapered coupler attached to the chip as shown in Fig. 2D (see Materials and Methods). The radiated beam is received by another standard WR 2.8 horn antenna in the far field at an over-the-air distance of 4.5 cm. We observe a flat broadband radiation response of the TA, shown by the nearly constant gain of 12.2 dBi over a spectral band from 0.31 to 0.34 THz in Fig. 2E, with frequency-dependent radiation angle θ(ω) in an angular range of 10°. The antenna gain evaluation method is discussed in the Supplementary Materials (fig. S4). Furthermore, the 200-μm-thick silicon membrane transmits the terahertz wave into both in-plane (*xy* plane) and out-of-plane (*z-direction*) directions, where the three-dimensional (3D) radiation pattern is plotted in Fig. 2F against both azimuth and elevation angles. The radiated energy is confined at an elevation HMAW of 49°. The radiated and total efficiencies are higher than 95% within the operation band (fig. S5), largely exceeding the electronic antenna efficiencies at terahertz (table S1). The TA is immune to sharp bends in the waveguide path (fig. S6).

Accurately controlling the direction of the terahertz beam emitted from the chip is critical for a wide range of applications including wireless communication, high-resolution imaging, and radar systems. The proposed device also enables the beam steering functionality by shifting the position of semicircular GRIB along the VPC-GRIB interface as shown in Fig. 3A. When the terminal point O of the VPC waveguide and the semicircle center O' of GRIB coincide, $\vec{k}_G$ and $\vec{k}'_G$ are pointing radially to the circular edge, collinear with $\vec{k}_A$ in free space. While a displacement between O and O' is introduced by shifting the position of GRIB, an additional refraction angle ψ (Fig. 3A) occurs due to the oblique incidence of wave on the circular edge, leading to a tunable azimuth angle $\theta' = \theta \pm \psi$. By moving GRIB along $\vec{e}_t$, a beam steering at an angle range of 36° is achieved, as indicated by the experimental gain spectra in Fig. 3 (B to D). We fabricated five different TA chips with OO' distances of −2.25, −1, 0, 1, and 2.25 mm. The constant n of GRIB-I results in both unaffected maximum gain and stable broadband responses, albeit OO' is shifted. Figure 3B shows the measured gain of over 12 dBi for each antenna at 0.325 THz as a

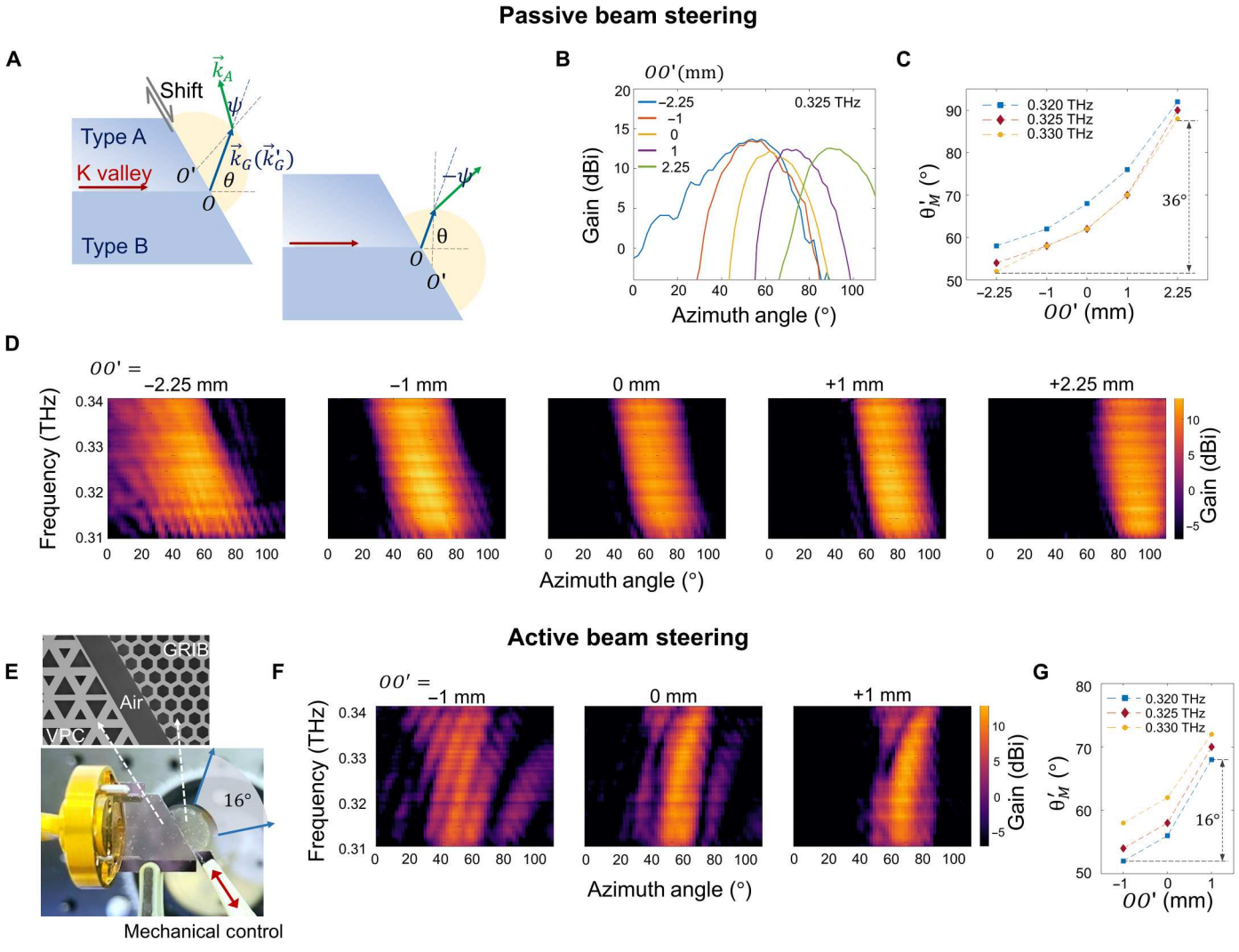

Fig. 3. Beam steering with the TA. (**A**) Schematic of TA beam steering. The edge region of the semicircular GRIB refracts the beam with an additional angle ±ψ by changing the VPC-GRIB displacement *OO*′. The topological valley momentum is adiabatically coupled into $\vec{k}_G$, $\vec{k}'$ (blue arrow) and eventually to $\vec{k}_A$ (green arrow) at a steered angle. (**B**) Radiation envelopes of steered angle-resolved beam at 0.325 THz. By fabricating five antenna chips with *OO*′ of −2.25, −1, 0, 1, and 2.25 mm, the radiation angles are passively tuned. (**C**) Tuned angles of maximum-gain θ'_M of the samples in (B) at 0.32, 0.325, and 0.33 THz, respectively. The tunable θ'_M is in a range of 36° with a 4.5-mm shift as exemplified at 0.33 THz. (**D**) Broadband responses of beam steering for the samples in (B) from 0.31 to 0.34 THz. (**E**) Schematic of active beam steering and optical image of separated VPC and GRIB. By shifting the position of GRIB mechanically, the radiation beam is steered actively by an angular range of 16°. (**F**) Active beam steering results from 0.31 to 0.34 THz with attenuated maximum gain over 9.7 dBi when *OO*′ is −1, 0, and 1 mm, respectively. (**G**) Tuned maximum-gain angle θ'_M at 0.32, 0.325, and 0.33 THz with an angular range of 16° within the representative displacement length of *OO*′ = 2 mm under active control.

function of azimuth angle. The azimuth angle of maximum-gain θ'_M changes from 52° for *OO*′ = −2.25 mm to 88° for *OO*′ = +2.25 mm, which is also plotted in Fig. 3C together with θ'_M at 0.32 and 0.33 THz. The broadband beam steering characteristics are illustrated in Fig. 3D. In the frequency range of 0.31 to 0.34 THz, the maximum antenna gain values are constantly over 12 dBi at varying angles.

In addition to the passive beam steering technique, we demonstrate an active approach to steer the terahertz beam by mechanically moving GRIB. We fabricated a pair of separated semicircular GRIB and VPC chips that are mounted on the mechanical translation stage, as displayed in Fig. 3E. By precisely translocating GRIB along the interface, the maximum-gain angle θ'_M is tuned as shown in Fig. 3F. Despite the altered angle dispersions between the passive (Fig. 3D) and active (Fig. 3F) experiments resulting from the imperfect position due to the air gap (~50 μm) between VPC and GRIB, the actively steered beams present broadband gain up to 9.7 dBi from 0.31 to 0.34 THz. The maximum-gain angle versus *OO*′ is shown in Fig. 3G at 0.32, 0.325, and 0.33 THz, respectively, where the total beam steering range achieved in real-time is 16° with a representative 2-mm shifting. Furthermore, active beam steering functionality is possibly achieved by changing the effective *n* using phase change materials or microelectromechanical cantilevers, such as GST (*30*) or MEMS (*31*).

The interchip valley momentum conservation is extremely important for maintaining robust characteristics between two topological VPC chips. The over-the-air valley conservation is

experimentally demonstrated by the first terahertz wireless communication between topological chips (setup is referred to Materials and Methods). Figure 4A shows the chip-air-chip transmissions, measured for various over-the-air distances d as shown in the top-right inset. With d ranging from 3.5 to 130.5 mm, the transmission results indicate a clear bandpass filtering in the range of 0.31 to 0.34 THz. The antenna gain response is also measured using interchip setup (also see Fig. S4), and the results are displayed in Fig. 4B. The gain remains constant in the far-field distance up to d = 500 mm, while the gain value increases in the near-field region (blue region) within 42 mm. The group delays of the interchip channel are measured at various distances from 3.5 to 130.5 mm, as shown in Fig. 4C, where each of them is nearly constant within a bandwidth of 25 GHz (0.315 to 0.34 THz). The group delay value of the tested TA is measured as 0.23 ns at 0.325 THz (fig. S7). Such constant group delay gives rise to the simultaneous transmission of modulated symbols to achieve data rate close to terabits per second, which is the result of valley-conserved chip-air-chip mode conversion. In addition, the TA ensures highly polarized (TE-polarized) wireless transmission with a 99% degree of polarization, enabling polarization multiplexing within the terahertz range, and ultimately increasing the overall spectral efficiency (fig. S8).

The interchip data communication experiments are performed at data speeds of 20, 50, and 100 Gbps, of those the measured error vector magnitude (EVM) results are plotted in Fig. 4 (D to F), respectively. The terahertz signal is generated by the unitraveling carrier photodiode (UTC-PD) and modulated by in-phase and quadrature (IQ) modulation (see Materials and Methods). The EVMs are recorded against the relative carrier signal power of UTC-PD. The reference EVM (black curve) is obtained when the UTC-PD is directly connected to the receiver for a fixed data rate, which requires the minimum relative power. The power penalty of the interchip wireless link is indicated by the corresponding horizontal shift from the reference curve for various over-the-air distances. In Fig. 4D, the 20-Gbps data rate with a 5 Gbaud symbol rate is performed at d of 3.5, 12, 42, and 80 mm, respectively, where the furthest free space distance can reach 80 mm. Figure 4 (E and F) illustrates EVM results for higher data speeds, where the furthest distances are 42 mm for 50 Gbps data rate and 12 mm for 100 Gbps, respectively. The representative IQ constellation diagrams with 16 quadrature amplitude modulation are also displayed as insets in Fig. 4 (D to F). It should be noted that the data speed and the over-the-air distance are limited by both the available terahertz source power and the sensitivity of the receiver. The valley-conserved interchip group delay remains constant even beyond the measurable distance (i.e., the group delay remains constant at 130.5 mm in Fig. 4C). A TA array can enhance the antenna gain and thereby extend the range for data delivery (fig. S9). Theoretically, a gain of 33 dBi can be achieved using a 10-element array, featuring an aperture size of 17 mm × 0.2 mm. When paired with electronic power amplifiers, it could enable significant data delivery over kilometer-scale distances while preserving signal quality.

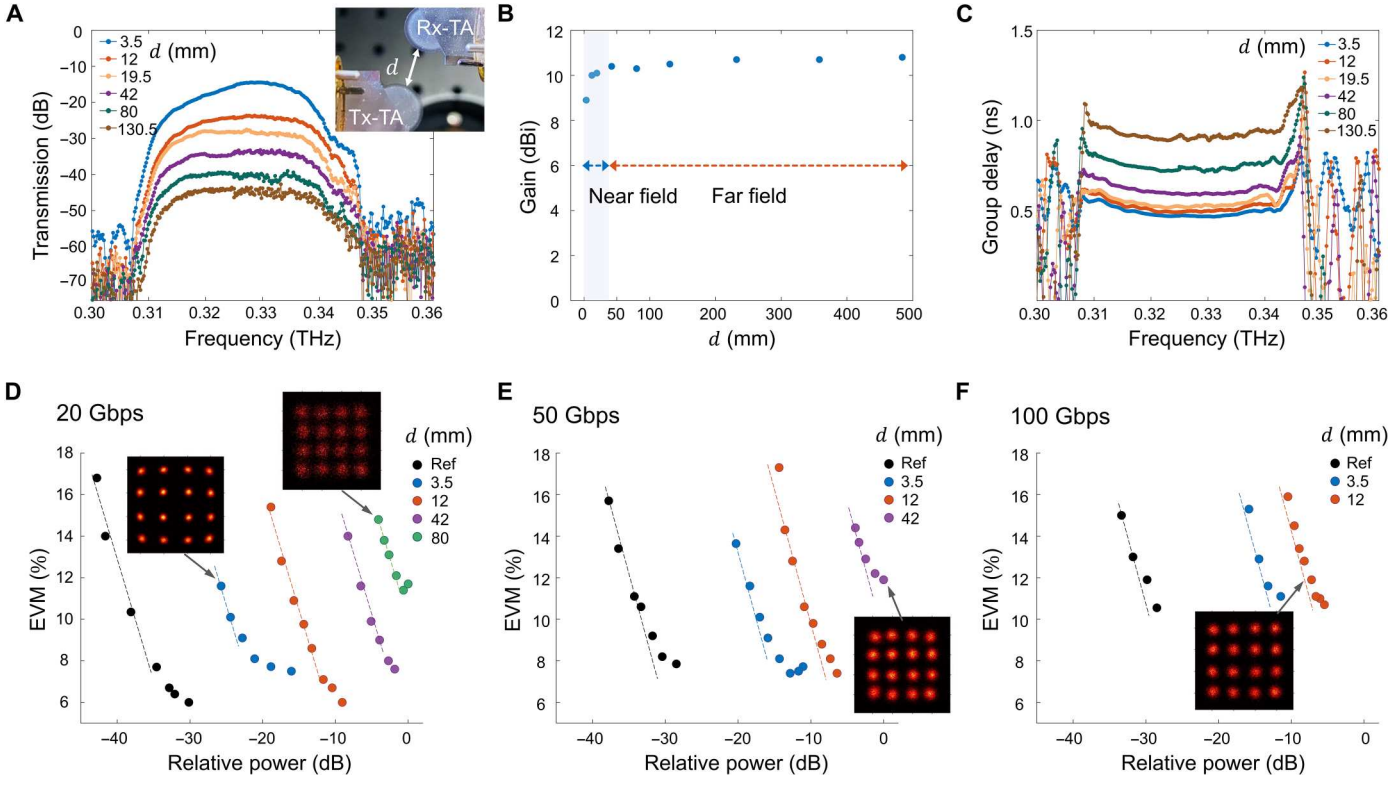

Fig. 4. Valley-conserved topodevices for interchip wireless terahertz communication. (**A**) Transmissions of the chip-air-chip channel for over-the-air d from 3.5 to 130.5 mm, showing a filtered band from 0.31 to 0.34 THz. d is shown in the inset of the interchip link. (**B**) Measured antenna gain using chip pair versus d at 0.325 THz. The near-field (blue region) and far-field regions are divided at d = 42 mm. (**C**) Measured constant group delays from 0.315 to 0.34 THz against d from 3.5 to 130.5 mm. (**D** to **F**) EVMs for data rates of 20, 50, and 100 Gbps with the carrier frequency of 0.325 THz, together with the representative IQ constellation diagrams. The EVMs are shown against the relative feeding power with the furthest measurable distances of 80, 42, and 12 mm, respectively.

DISCUSSION

In summary, we have presented terahertz wireless communication using valley-conserved topological waveguide antenna devices for 6G to XG communications. Our TA maintains a stable gain of 12.2 dBi over a 30-GHz frequency bandwidth and allows for active control of the terahertz radiation beam direction without compromising its gain performance. The wireless data communication experiment demonstrated a remarkable data speed of 100 Gbps, made possible by the constant group delays resulting from the interchip valley conservation. The significance of our discovery lies in the development of a valley-conserved momentum matching strategy for all topological photonic devices, which is critical for efficient topological edge state transition regardless of highly contrasting eigen wavevectors. Our proposed topological wireless communication system unlocks the opportunities for the development of highly efficient and high-speed wireless technology with a primary focus on backhaul applications in sixth-generation networks. The wireless link has the potential to be scaled into the infrared frequency band for ultra-broadband communication, opening possibilities in various fields such as telecommunications, data centers, and computing.

MATERIALS AND METHODS

The TA is fabricated on a 200-μm-thick high-resistivity silicon (>10,000 ohm·cm) wafer. A 2-μm-thick silicon-dioxide layer is first deposited on the top of the wafer. The 1.5-μm-thick photoresist AZ 5214E is coated and patterned using photolithography. The reactive ion etching (RIE) is carried out to etch the silicon-dioxide hardcover. The accurate deep reactive ion etching (DRIE) on silicon is performed to penetratingly pattern air holes with multiple aspect ratios for the chip integrating VPC and GRIB.

For characterizing the TA, the Virginia Diodes Inc. (VDI) frequency extension model (WR2.8SGX, 260 to 400 GHz) upconverts microwave signal from a signal generator (Keysight PSG Analog Signal Generator, 250 kHz to 20 GHz) into a 0.325-THz frequency band. The terahertz wave is coupled into the silicon chip from the WR-2.8 hollow waveguide (WM-710, 260 to 400 GHz) through the silicon tapered coupler attached to the sample. A WR 2.8 diagonal horn antenna, oriented using a motor-driven rotational stage, is used to receive the radiated terahertz beam. The received terahertz signal is down-converted with the VDI spectrum analyzer extension module (WR2.8SAX, 260 to 400 GHz) and displayed using a spectrum analyzer (Keysight EXA Signal Analyzer, 10 Hz to 32 GHz). The signal generator, spectrum analyzer, and rotational stage are integrated and controlled through LABVIEW for precise measurement control and acquisition, based on which the angle-resolved antenna gain is obtained. The active mechanical control is achieved by two sample holders on parallel moving stages. For the 3D scanning system, a combination of multiplication chain and equivalent 20-GHz synthesizer was used at the transmitter and standard Schottky diode for detection. The distance between the tested TA and the received antenna was in the far-field distance of 200 mm. All the instruments were controlled by LABVIEW software.

For interchip communication, two continuous lasers at 1550 nm are combined with a fiber coupler to generate terahertz carrier frequency. One of the laser lines is fixed as a reference, while the other one is modulated with an IQ modulator whose frequency is separated by 0.325 THz. The optical signal is then amplified with erbium-doped fiber amplifier and down-converted from the optical to the terahertz domain using UTC-PD. This modulated terahertz carrier is coupled into the TA using a WR 3.4 waveguide. The terahertz wireless gap is linked by the TA-air-TA channel. The output terahertz signal is collected into a second standard WR 3.4 waveguide and further downconverted by a subharmonic mixer into a lower frequency. The signal is then amplified by an SHF-810 amplifier and further analyzed by a real-time oscilloscope (70 GHz), based on which the performance of interchip transmission, the overall group delay, the IQ constellation map, and the EVMs are evaluated.

The band diagrams of the VPC unit cell, the topological kink state, the GRIB mode, and the wave in the air are calculated with a finite-element method (COMSOL Multiphysics) using 2D simulations. The numerical antenna gain spectra and the field profile of the antenna are achieved by a time domain solver with finite integration theory (CST Studio Suite) in 3D. The data processing is carried out with MATLAB.

Supplementary Materials

This PDF file includes:

Supplementary Text
Figs. S1 to S9
Table S1
References

REFERENCES AND NOTES

1. M. Z. Hasan, C. L. Kane, Colloquium: Topological insulators. *Rev. Mod. Phys.* **82**, 3045–3067 (2010).
2. J. E. Moore, The birth of topological insulators. *Nature* **464**, 194–198 (2010).
3. A. B. Khanikaev, S. Hossein Mousavi, W.-K. Tse, M. Kargarian, A. H. MacDonald, G. Shvets, Photonic topological insulators. *Nat. Mater.* **12**, 233–239 (2013).
4. L. Lu, J. D. Joannopoulos, M. Soljačić, Topological photonics. *Nat. Photonics* **8**, 821–829 (2014).
5. H. Xue, Y. Yang, B. Zhang, Topological acoustics. *Nat. Rev. Mater.* **7**, 974–990 (2022).
6. T. Ma, G. Shvets, All-Si valley-Hall photonic topological insulator. *New J. Phys.* **18**, 025012 (2016).
7. J.-W. Dong, X.-D. Chen, H. Zhu, Y. Wang, X. Zhang, Valley photonic crystals for control of spin and topology. *Nat. Mater.* **16**, 298–302 (2017).
8. Y. Yang, Y. Yamagami, X. Yu, P. Pitchappa, J. Webber, B. Zhang, M. Fujita, T. Nagatsuma, R. Singh, Terahertz topological photonics for on-chip communication. *Nat. Photonics* **14**, 446–451 (2020).
9. A. Kumar, M. Gupta, P. Pitchappa, N. Wang, M. Fujita, R. Singh, Terahertz topological photonic integrated circuits for 6G and beyond: A perspective. *J. Appl. Phys.* **132**, 140901 (2022).
10. L. Zhang, Y. Yang, M. He, H.-X. Wang, Z. Yang, E. Li, F. Gao, B. Zhang, R. Singh, J.-H. Jiang, H. Chen, Valley kink states and topological channel intersections in substrate-integrated photonic circuitry. *Laser Photonics Rev.* **13**, 1900159 (2019).
11. Y. J. Tan, W. Wang, A. Kumar, R. Singh, Interfacial topological photonics: Broadband silicon waveguides for THz 6G communication and beyond. *Opt. Express* **30**, 33035–33047 (2022).
12. X. Wu, Y. Meng, J. Tian, Y. Huang, H. Xiang, D. Han, W. Wen, Direct observation of valley-polarized topological edge states in designer surface plasmon crystals. *Nat. Commun.* **8**, 1304 (2017).
13. L. He, H. Y. Ji, Y. J. Wang, X. D. Zhang, Topologically protected beam splitters and logic gates based on two-dimensional silicon photonic crystal slabs. *Opt. Express* **28**, 34015–34023 (2020).
14. X. Xie, S. Yan, J. Dang, J. Yang, S. Xiao, Y. Wang, S. Shi, L. Yang, D. Dai, Y. Yuan, N. Luo, T. Cui, G. Chi, Z. Zuo, B.-B. Li, C. Wang, X. Xu, Topological cavity based on slow-light topological edge mode for broadband Purcell enhancement. *Phys. Rev. Appl.* **16**, 014036 (2021).
15. A. Kumar, M. Gupta, P. Pitchappa, T. C. Tan, U. Chattopadhyay, G. Ducournau, N. Wang, Y. Chong, R. Singh, Active ultrahigh-Q (0.2×10^6) THz topological cavities on a chip. *Adv. Mater.* **34**, e2202370 (2022).

16. Y. Zeng, U. Chattopadhyay, B. Zhu, B. Qiang, J. Li, Y. Jin, L. Li, A. G. Davies, E. H. Linfield, B. Zhang, Y. Chong, Q. J. Wang, Electrically pumped topological laser with valley edge modes. *Nature* **578**, 246–250 (2020).
17. Y. Gong, S. Wong, A. J. Bennett, D. L. Huffaker, S. S. Oh, Topological insulator laser using valley-hall photonic crystals. *ACS Photonics* **7**, 2089–2097 (2020).
18. T. Nagatsuma, G. Ducournau, C. C. Renaud, Advances in terahertz communications accelerated by photonics. *Nat. Photonics* **10**, 371–379 (2016).
19. K. Tsuruda, M. Fujita, T. Nagatsuma, Extremely low-loss terahertz waveguide based on silicon photonic-crystal slab. *Opt. Express* **23**, 31977–31990 (2015).
20. D. Headland, W. Withayachumnankul, R. Yamada, M. Fujita, T. Nagatsuma, Terahertz multibeam antenna using photonic crystal waveguide and Luneburg lens. *APL Photonics* **3**, 126105 (2018).
21. J. Webber, Y. Yamagami, G. Ducournau, P. Szriftgiser, K. Iyoda, M. Fujita, T. Nagatsuma, R. Singh, Terahertz band communications with topological valley photonic crystal waveguide. *J. Light. Technol.* **39**, 7609–7620 (2021).
22. A. Kumar, M. Gupta, P. Pitchappa, N. Wang, P. Szriftgiser, G. Ducournau, R. Singh, Phototunable chip-scale topological photonics: 160 Gbps waveguide and demultiplexer for THz 6G communication. *Nat. Commun.* **13**, 5404 (2022).
23. I. F. Akyildiz, C. Han, Z. Hu, S. Nie, J. M. Jornet, Terahertz band communication: An old problem revisited and research directions for the next decade. *IEEE Trans. Commun.* **70**, 4250–4285 (2022).
24. S. Koenig, D. Lopez-Diaz, J. Antes, F. Boes, R. Henneberger, A. Leuther, A. Tessmann, R. Schmogrow, D. Hillerkuss, R. Palmer, T. Zwick, C. Koos, W. Freude, O. Ambacher, J. Leuthold, I. Kallfass, Wireless sub-THz communication system with high data rate. *Nat. Photonics* **7**, 977–981 (2013).
25. A.-A. A. Boulogeorgos, A. Alexiou, T. Merkle, C. Schubert, R. Elschner, A. Katsiotis, P. Stavrianos, D. Kritharidis, P.-K. Chartsias, J. Kokkoniemi, M. Juntti, J. Lehtomaki, A. Teixeira, F. Rodrigues, Terahertz technologies to deliver optical network quality of experience in wireless systems beyond 5G. *IEEE Commun. Mag.* **56**, 144–151 (2018).
26. T. Harter, C. Füllner, J. N. Kemal, S. Ummethala, J. L. Steinmann, M. Brosi, J. L. Hesler, E. Bründermann, A.-S. Müller, W. Freude, S. Randel, C. Koos, Generalized Kramers–Kronig receiver for coherent terahertz communications. *Nat. Photonics* **14**, 601–606 (2020).
27. Y. Ghasempour, R. Shrestha, A. Charous, E. Knightly, D. M. Mittleman, Single-shot link discovery for terahertz wireless networks. *Nat. Commun.* **11**, 2017 (2020).
28. J. M. Jornet, E. W. Knightly, D. M. Mittleman, Wireless communications sensing and security above 100 GHz. *Nat. Commun.* **14**, 841 (2023).
29. F. Gao, H. Xue, Z. Yang, K. Lai, Y. Yu, X. Lin, Y. Chong, G. Shvets, B. Zhang, Topologically protected refraction of robust kink states in valley photonic crystals. *Nat. Phys.* **14**, 140–144 (2018).
30. S. Abdollahramezani, O. Hemmatyar, M. Taghinejad, H. Taghinejad, A. Krasnok, A. A. Eftekhar, C. Teichrib, S. Deshmukh, M. A. El-Sayed, E. Pop, M. Wuttig, A. Alù, W. Cai, A. Adibi, Electrically driven reprogrammable phase-change metasurface reaching 80% efficiency. *Nat. Commun.* **13**, 1696 (2022).
31. N. Quack, H. Sattari, A. Y. Takabayashi, Y. Zhang, P. Verheyen, W. Bogaerts, P. Edinger, C. Errando-Herranz, K. B. Gylfason, MEMS-enabled silicon photonic integrated devices and circuits. *IEEE J. Quantum Electron.* **56**, 1–10 (2020).
32. D. Headland, M. Fujita, T. Nagatsuma, Half-Maxwell fisheye lens with photonic crystal waveguide for the integration of terahertz optics. *Opt. Express* **28**, 2366–2380 (2020).
33. D. Hou, J. Chen, P. Yan, W. Hong, A 270 GHz × 9 multiplier chain MMIC with on-chip dielectric-resonator antenna. *IEEE Trans. Terahertz Sci. Technol.* **8**, 224–230 (2018).
34. K. Guo, Y. Zhang, P. Reynaert, A 0.53-THz subharmonic injection-locked phased array with 63-μ W radiated power in 40-nm CMOS. *IEEE J. Solid-State Circuits* **54**, 380–391 (2019).
35. L. Gao, C. H. Chan, A 0.47-THz ring scalable coupled oscillator–radiator array with miniature patch antennas. *IEEE Trans. Microw. Theory Tech.* **70**, 3964–3974 (2022).
36. S. Sinha, M. Libois, K. Vaesen, H. Suys, L. Pauwels, I. Ocket, Miniaturized (127 to 154) GHz dipole arrays in 28 nm bulk CMOS with enhanced efficiency. *IEEE Trans. Antennas Propag.* **69**, 1414–1426 (2021).
37. V. Lammert, M. Leyrer, M. Hamouda, R. Weigel, V. Issakov, Dual-mode substrate wave cancellation in a 120 GHz 2 × 2 on-chip dipole array. *IEEE Trans. Antennas Propag.* **70**, 6683–6691 (2022).
38. H. Saeidi, S. Venkatesh, C. R. Chappidi, T. Sharma, C. Zhu, K. Sengupta, A 4 × 4 steerable 14-dBm EIRP array on CMOS at 0.41 THz with a 2D distributed oscillator network. *IEEE J. Solid-State Circuits* **57**, 3125–3138 (2022).
39. H. Jalili, O. Momeni, A 0.46-THz 25-element scalable and wideband radiator array with optimized lens integration in 65-nm CMOS. *IEEE J. Solid-State Circuits* **55**, 2387–2400 (2020).
40. P. Sen, J. V. Siles, N. Thawdar, J. M. Jornet, Multi-kilometre and multi-gigabit-per-second sub-terahertz communications for wireless backhaul applications. *Nat. Electron.* **6**, 164–175 (2023).

Acknowledgments

Funding: All the authors acknowledge the research funding support from the National Research Foundation (NRF) Singapore (grant no. NRF-CRP23-2019-0005, TERACOMM). G.D. and P.S. acknowledge the support from 'France 2030' programs, PEPR (Programmes et Equipements Prioritaires pour la Recherche), and CPER Wavetech. The PEPR is operated by the Agence Nationale de la Recherche (ANR), under the grants ANR-22-PEEL-0006 (FUNTERA, PEPR 'Electronics') and ANR-22-PEFT-0006 (NF-SYSTERA, PEPR 5G and beyond - Future Networks). The Contrat de Plan Etat-Region (CPER) WaveTech is supported by the Ministry of Higher Education and Research, the Hauts-de-France Regional council, the Lille European Metropolis (MEL), the Institute of Physics of the French National Centre for Scientific Research (CNRS) and the European Regional Development Fund (ERDF). **Author contributions:** Conceptualization: R.J., A.K., M.G., and R.S. Methodology: R.J., A.K., and Y.J.T. Investigation: R.J., S.K., T.C.T., P.S., A.A., and G.D. Visualization: R.J. Supervision: R.S. Writing—original draft: R.J., G.D., and R.S. Writing—review and editing: R.J., S.K., Y.J.T., and R.S. **Competing interests:** The authors declare that they have no competing interests. **Data and materials availability:** All data needed to evaluate the conclusions in the paper are present in the paper and/or the Supplementary Materials.

Submitted 22 May 2023
Accepted 29 September 2023
Published 1 November 2023
10.1126/sciadv.adi8500

ScienceAdvances

Valley-conserved topological integrated antenna for 100-Gbps THz 6G wireless

Ridong Jia, Sonu Kumar, Thomas Caiwei Tan, Abhishek Kumar, Yi Ji Tan, Manoj Gupta, Pascal Szriftgiser, Arokiaswami Alphones, Guillaume Ducournau, and Ranjan Singh

Sci. Adv. **9** (44), eadi8500. DOI: 10.1126/sciadv.adi8500

Science Advances (ISSN 2375-2548) is published by the American Association for the Advancement of Science. 1200 New York Avenue NW, Washington, DC 20005. The title *Science Advances* is a registered trademark of AAAS.